Supporting Information for "Accurate Modeling of Interfacial Thermal Transport in van der Waals Heterostructures via Hybrid Machine Learning and Registry-Dependent Potentials"

Wenwu Jiang,[1#] Hekai Bu,[1#] Ting Liang,[2#] Penghua Ying,[3] Zheyong Fan,[4] Jianbin Xu,[2] Wengen Ouyang[1,5*]

[1]*Department of Engineering Mechanics, School of Civil Engineering, Wuhan University, Wuhan, Hubei 430072, China*

[2]*Department of Electronic Engineering and Materials Science and Technology Research Center, The Chinese University of Hong Kong, Shatin, N.T., Hong Kong SAR, 999077, P. R. China*

[3]*Department of Physical Chemistry, School of Chemistry, Tel Aviv University, Tel Aviv 6997801, Israel*

[4]*College of Physical Science and Technology, Bohai University, Jinzhou 121013, China*

[5]*State Key Laboratory of Water Resources Engineering and Management, Wuhan University, Wuhan, Hubei 430072, China*

[#]These authors contribute equally to this work.

[*]Corresponding authors. Email: w.g.ouyang@whu.edu.cn

This supporting information document includes the following sections:

1. Details of NEP Model Training

1.1. Hyperparameters for NEP training

The NEP models can be trained using the neuroevolution potential *nep* executable in the GPUMD package.[1] The relevant hyperparameters are specified in the *nep.in* input file. The contents of the *nep.in* input file for training the NEP(5 Å, 5 Å) model of MX_2 (where M = Mo/W and X = S/Se/Te) are given below. Since long-range dispersion forces can be captured by interlayer potential or D3, radial and angular cutoffs can be relatively small.

```
type 2 Mo S # parameter can be modified depending on the specific MX2 system.
version 4 # version 4
cutoff 5 5
n_max 8 8
basis_size 12 12
l_max 4 2 0
neuron 50
lambda_e 1.0
lambda_f 1.0
lambda_v 0.1
batch 10000
population 50
generation 1000000
```

1.2. NEP training results

By performing single-point DFT calculations on these configurations, we trained their energy, force, and stress using the NEP model. As shown in **Figures S1**-**S6**, the NEP predicted data matches the DFT reference data very well. The calculated root-mean-square error (RMSE) is very small, indicating that the NEP model has high accuracy.

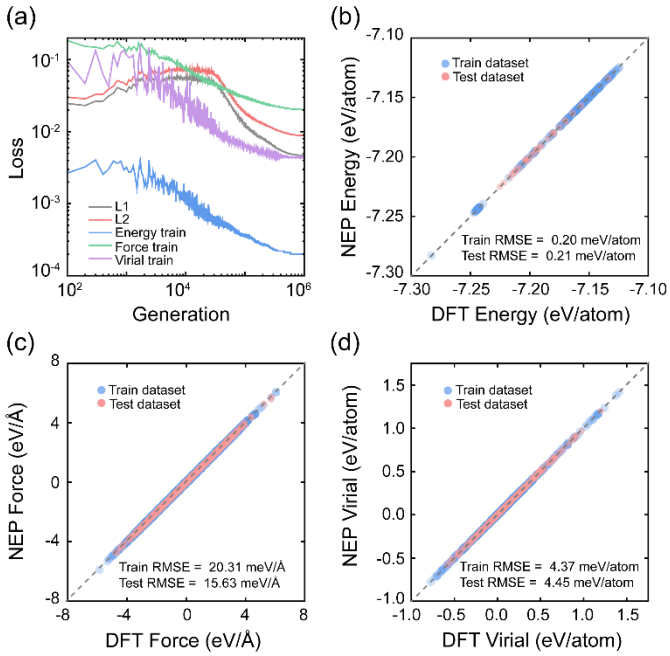

Figure S1. (a) Evolution of the various terms in the loss function for the MoS_2 training data set with respect to the generation. Parity plots for (b) total energies, (c) atomic forces obtained, and (d) virials for the NEP training data sets.

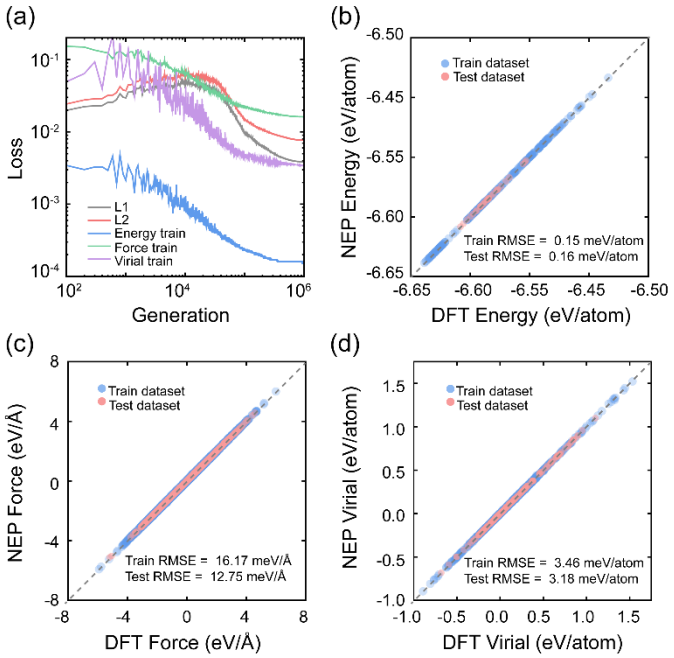

Figure S2. (a) Evolution of the various terms in the loss function for the $MoSe_2$ training data set with respect to the generation. Parity plots for (b) total energies, (c) atomic forces obtained, and (d) virials for the NEP training data sets.

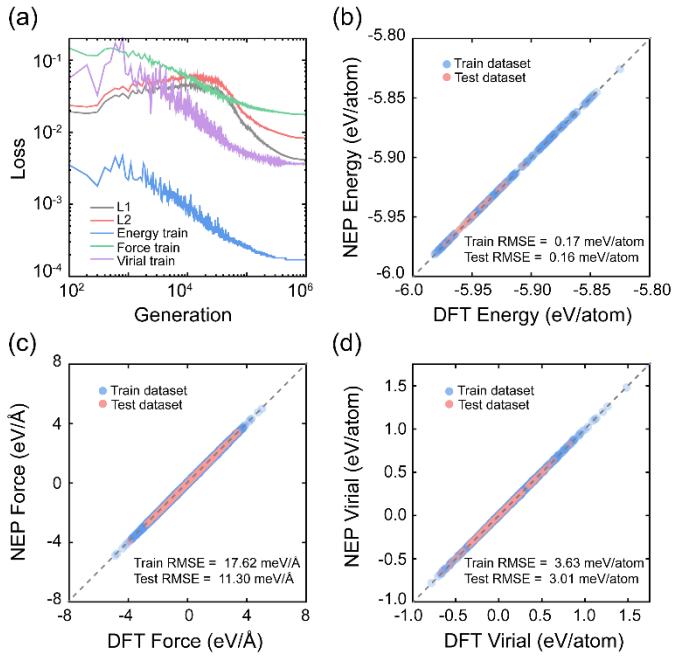

Figure S3. (a) Evolution of the various terms in the loss function for the $MoTe_2$ training data set with respect to the generation. Parity plots for (b) total energies, (c) atomic forces obtained, and (d) virials for the NEP training data sets.

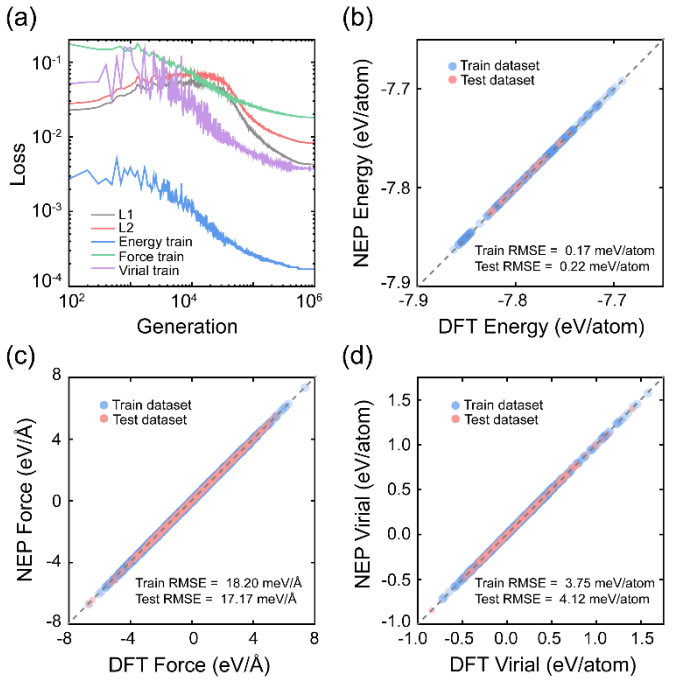

Figure S4. (a) Evolution of the various terms in the loss function for the WS_2 training data set with respect to the generation. Parity plots for (b) total energies, (c) atomic forces obtained, and (d) virials for the NEP training data sets.

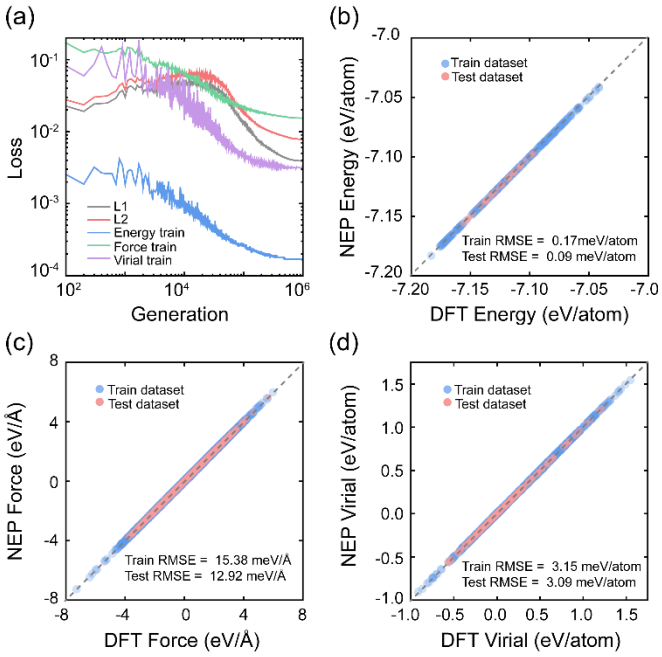

Figure S5. (a) Evolution of the various terms in the loss function for the WSe_2 training data set with respect to the generation. Parity plots for (b) total energies, (c) atomic forces obtained, and (d) virials for the NEP training data sets.

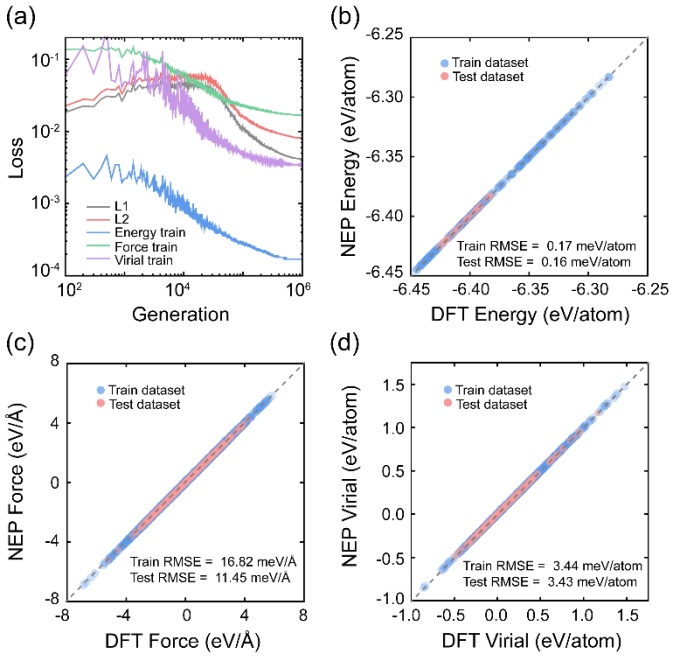

Figure S6. (a) Evolution of the various terms in the loss function for the WTe_2 training data set with respect to the generation. Parity plots for (b) total energies, (c) atomic forces obtained, and (d) virials for the NEP training data sets.

2. Details of Interlayer Potential Parameterization

2.1 ILP Parameterization of $MoTe_2$ and WTe_2

In our previous studies, we have parameterized the anisotropic interlayer potential to describe the interlayer interactions in homogeneous and heterogeneous interfaces of group-VI transition metal dichalcogenides (MX_2, where M = Mo, W, and X = S, Se).[2] However, the current force field did not account for transition metal tellurides ($MoTe_2$ and WTe_2). In this work, we further developed the ILP force fields for $MoTe_2$ and WTe_2. We computed the binding energy (BE) curves and sliding potential energy surfaces (PESs) for two homojunctions ($MoTe_2$ and WTe_2). Each BE curve and sliding PES contain 31 and 132 data points, respectively. All DFT reference data were calculated using the MBD-NL-augmented PBE functional,[3] as implemented in the FHI-AIMS code,[4] with the tier-2 basis-set, using tight convergence settings including all grid divisions and 974 outer grids. In order to balance the computational cost and accuracy, five high symmetry stacking modes (as shown in **Figure S7**), including two parallel configurations (AA and AB stacking) and three anti-parallel configurations (AA′, AB′, and A′B stacking), were utilized to calculate the binding energy curves and sliding potential energy surfaces.

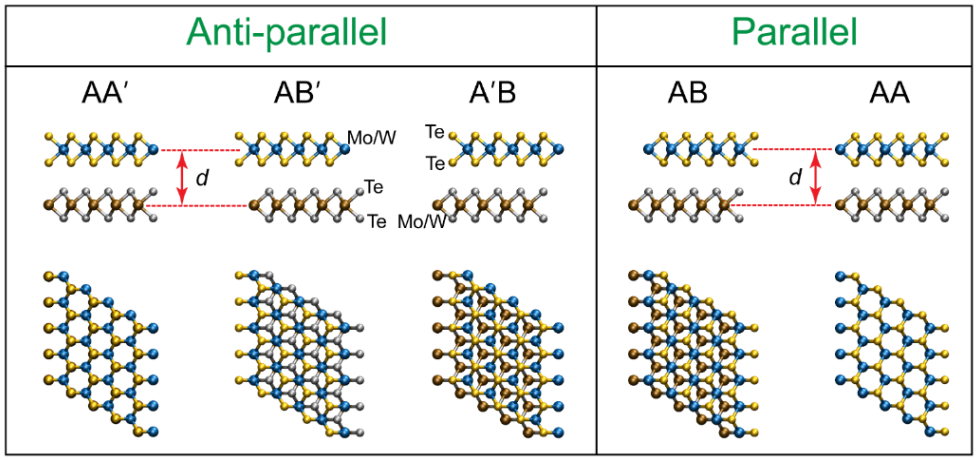

Figure S7. A typical configuration $MoTe_2/WTe_2$ with five high symmetry stacking modes considered herein, which includes two parallel configurations (AA and AB stackings) and three anti-parallel configurations (AA′, AB′, and A′B stackings). For clarity, tellurium, molybdenum, and tungsten atoms residing in different layers are marked with different colors as labeled. The interlayer distance, *d*, is defined as the distance between transition metal atoms of adjacent layers.

To ensure the accuracy of our computational findings, we first investigated the convergence of the DFT results by performing BE calculations with different vacuum sizes and *k*-grid densities for AA′-stacked bilayer $MoTe_2$ and WTe_2, while all other settings, including the convergence criteria of charge density and eigenvalues, are kept unchanged. The testing results are presented in Sec. 2.2. In addition, we also compared the BE and sliding energy barriers of $MoTe_2$ calculated using both HSE+MBD-NL and PBE+MBD-NL (See Sec. 2.3).

Figure S8 presents BE curves obtained using PBE+MBD-NL calculations (open symbols) and ILP (solid lines) for bilayer $MoTe_2$ (left column) and WTe_2 (right column) at interlayer distances ranging from 6-15 Å, respectively. Notably, both the homojunctions $MoTe_2$ and WTe_2 systems possess almost the same equilibrium interlayer distance (7.1 Å) of AA′-stacked model due to similar intrinsic attributes between $MoTe_2$ and WTe_2.

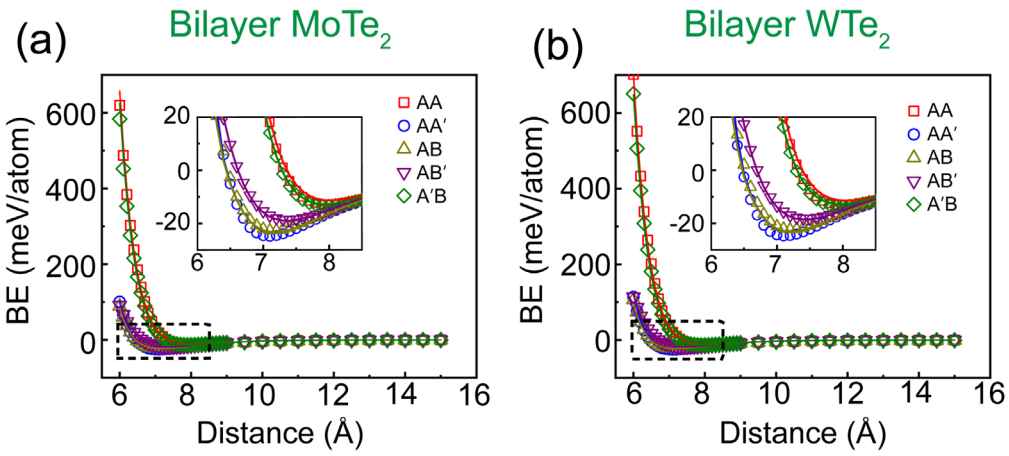

Figure S8. Binding energy curves of the laterally periodic structures of bilayer $MoTe_2$ (a) and WTe_2 (b) calculated using PBE+MBD-NL (open symbols), along with the corresponding ILP fits (solid lines). The reported energies are measured relative to the value obtained for infinitely separated layers and are normalized by the total number of atoms in the unit cell (6 atoms). The insets provide an enlarged view of the equilibrium interlayer distance region for five different stacked configurations.

The sliding PES of periodic bilayer $MoTe_2$ and WTe_2 with both anti-parallel and parallel configurations are presented in **Figure S9** and **Figure S10**, respectively. The left and middle panels demonstrate the sliding PES calculated using PBE+MBD-NL and ILP at the equilibrium

interlayer distances of the corresponding structure, respectively. While the right panels show the differences between the reference DTF data and the ILP prediction. Excellent qualitative and quantitative agreement between the ILP results and the DFT reference data for all systems is observed from those figures, showing differences within ~2 meV/atom.

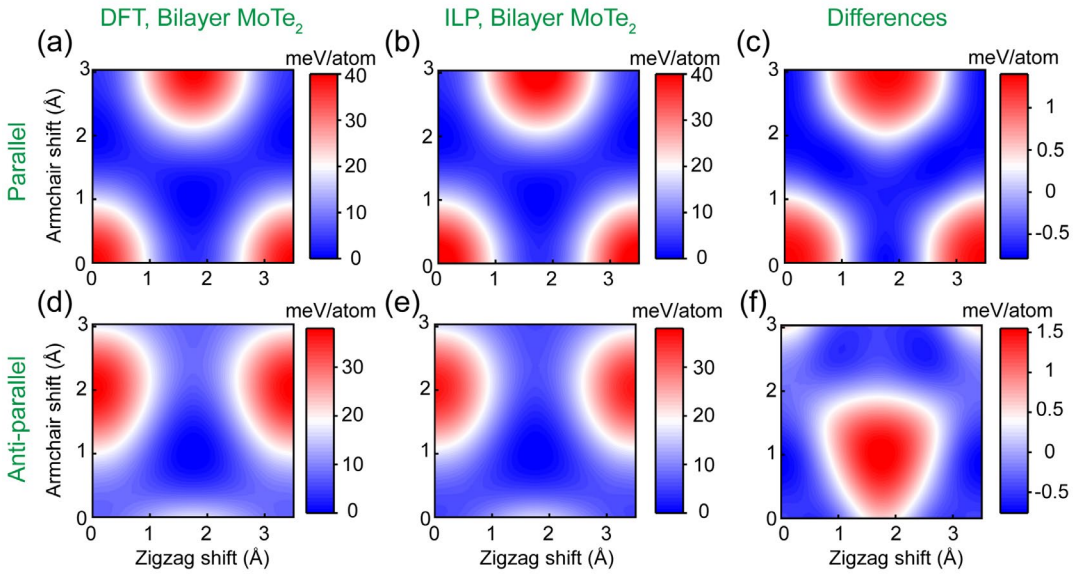

Figure S9. Sliding PESs of the laterally periodic bilayer $MoTe_2$, calculated at an interlayer distance of 7.1 Å for top panels (parallel configuration) and bottom panels (anti-parallel configuration). The first and second rows present the sliding PESs obtained for the parallel configuration and the anti-parallel configuration, calculated using PBE+MBD-NL (a, d) and the ILP (b, e). Panels (c) and (f) present the differences between the DFT results and the ILP calculations. All the energies are normalized by the total number of atoms in the unit cell (6 atoms).

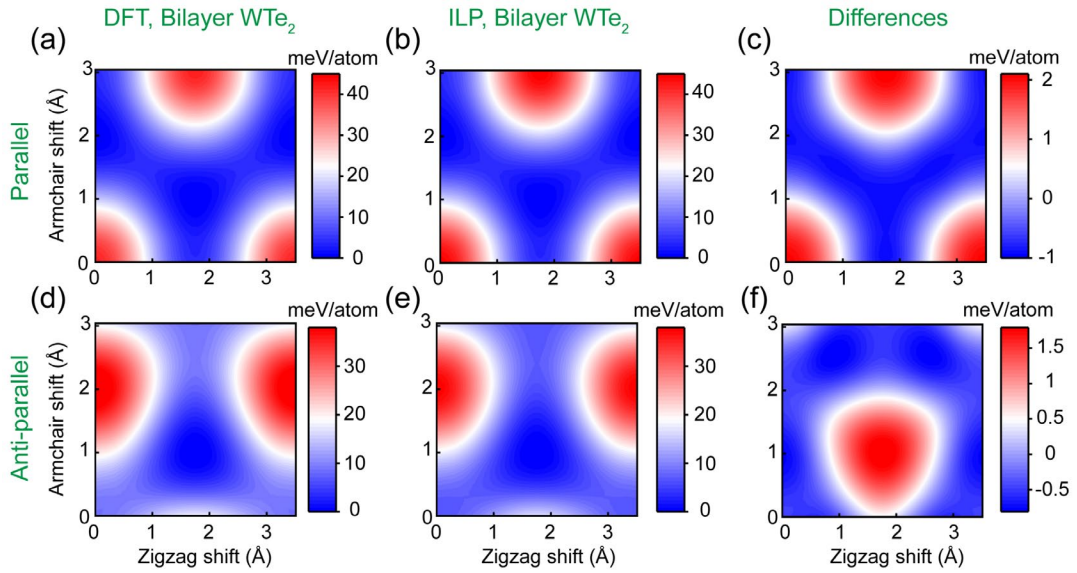

Figure S10. Sliding PESs of the laterally periodic bilayer WTe_2, calculated at an interlayer distance of 7.1 Å for top panels (parallel configuration) and bottom panels (anti-parallel configuration). The first and second rows present the sliding PESs obtained for the parallel configuration and the anti-parallel configuration, calculated using PBE+MBD-NL (a, d) and the ILP (b, e). Panels (c) and (f) present the differences between the DFT results and the ILP calculations. All the energies are normalized by the total number of atoms in the unit cell (6 atoms).

2.2 Convergence Tests of the Reference DFT Calculations

In previous work, we found that achieving convergence of the DFT reference results depends on the appropriate selection of vacuum size and the *k*-grid density. To ensure convergence of the DFT results, we performed a series of binding energy (BE) calculations with different vacuum sizes and *k*-grid densities for both bilayer $MoTe_2$ and WTe_2 systems. **Figure S11** and **Figure S12** present the BE convergence of $MoTe_2$ and WTe_2 with respect to vacuum size and *k*-grid density, respectively, where the red color marks the parameters employed to generate the reference results in the main text. The rest of the parameters are kept the same as detailed in the main text. It can be seen that a vacuum size of 100 Å and a *k*-point grid of 19×19×1 give good BE convergence of ~0.05 meV/atom.

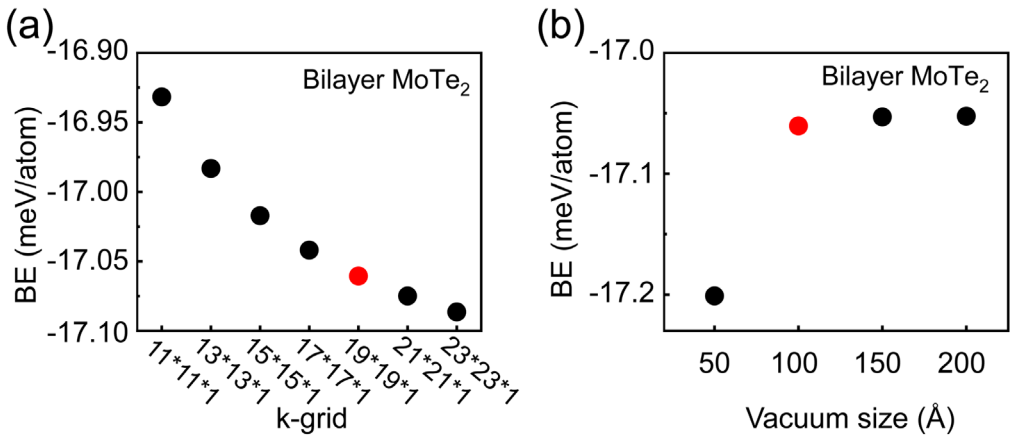

Figure S11. BE convergence tests for AA′-stacked bilayer $MoTe_2$ with respect to *k*-grid density (a) and vacuum size (b). The vacuum size in (a) was fixed at 100 Å and the *k*-grid in (b) was chosen as 19×19×1. In both cases, the interlayer distance was fixed at 7.1 Å. Notably, all subsequent results for $MoTe_2$ presented in the following sections were calculated using the values marked with red symbols.

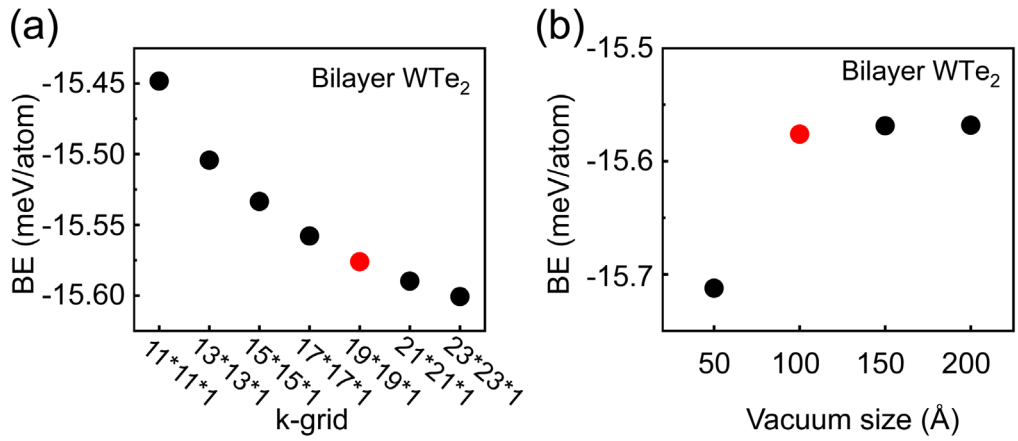

Figure S12. BE convergence tests for AA′-stacked bilayer WTe_2 with respect to *k*-grid density (a) and vacuum size (b). The vacuum size in (a) was fixed at 100 Å and the *k*-grid in (b) was chosen as 19×19×1. In both cases, the interlayer distance was fixed at 7.1 Å. Notably, all subsequent results for WTe_2 presented in the following sections were calculated using the values marked with red symbols.

2.3 Effect of DFT Method on Binding Energy of TMD Bilayers

In this section, we investigated the influence of different DFT methods, specifically Heyd−Scuseria−Ernzerhof (HSE) and Perdew-Burke-Ernzerhof (PBE) density functional

approximations, on the BE and sliding energy barriers of bilayer $MoTe_2$. All DFT calculations were enhanced with non-local many-body dispersion (MBD-NL) long-range corrections. The binding energies calculated for bilayer AA′-stacked $MoTe_2$ with the two DFT methods are illustrated in **Figure S13a**. The comparison shows the differences between the binding energies calculated using HSE+MBD-NL (black) and PBE+MBD-NL (red) are 3.78 meV/atom (~13.8%), 4.26 meV/atom (~14.6%), and 4.04 meV/atom (~14.5%) at interlayer distances of 6.9 Å, 7.1 Å, and 7.3 Å, respectively. **Figure S13b** shows the maximum sliding energy barriers at an interlayer distance of 7.1 Å for bilayer $MoTe_2$. The sliding energy barriers for parallel and antiparallel configurations calculated using PBE+MBD-NL (red) differ from those calculated using HSE+MBD-NL (black) by 5.49 meV/atom (~12%) and 2.86 meV/atom (~8%), respectively. From these results, we can confidently conclude that PBE+MBD-NL offers a reasonable level of accuracy compared to HSE+MBD-NL. It's worth noting that the computational cost associated with HSE+MBD-NL is approximately 400 times higher than that of PBE+MBD-NL. Therefore, PBE+MBD-NL serves as a cost-effective alternative method suitable for investigating $MoTe_2$ and WTe_2.

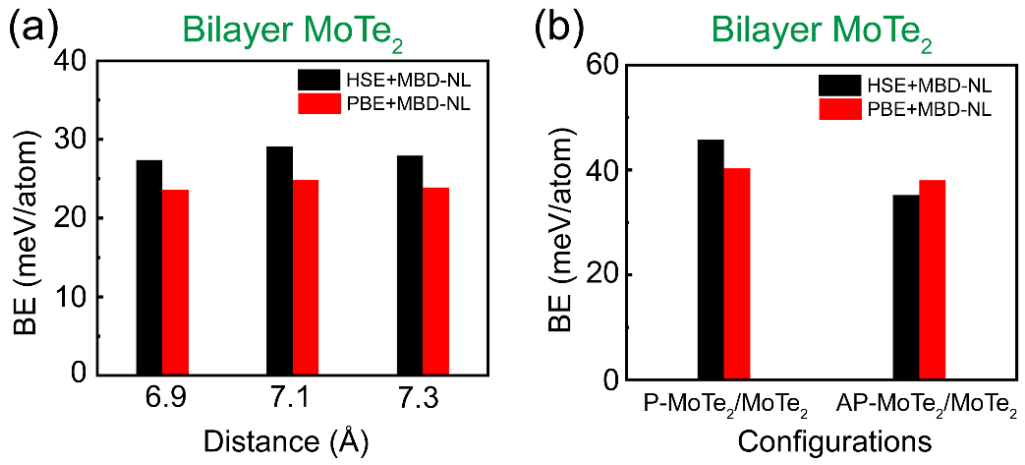

Figure S13. (a) Binding energy (a) at interlayer distances of 6.9, 7.1, and 7.3 Å for the AA′-stacked $MoTe_2$ bilayer and sliding energy barriers (b) under the interlayer distance of 7.1 Å (both parallel and antiparallel configurations) for bilayer $MoTe_2$ system calculated using HSE+MBD-NL (black) and PBE+MBD-NL (red).

2.4 The Local Normal Vectors

For a given atom i, the surface normal vector $\boldsymbol{n}_i$ is calculated with its six nearest neighboring atoms residing in the same sublayer (see **Figure S14**):

$$\boldsymbol{n}_i = \frac{\boldsymbol{N}_i}{|\boldsymbol{N}_i|}, \boldsymbol{N}_i = \frac{1}{6}\left[\sum_{k=1}^{6}\left(\boldsymbol{r}_{k,i} \times \boldsymbol{r}_{k+1,i}\right)\right], \tag{S1}$$

where $\boldsymbol{r}_{k,i} = \boldsymbol{r}_k - \boldsymbol{r}_i, k = 1,2,\cdots 6$, and the summation is cyclic with $\boldsymbol{r}_{7,i} = \boldsymbol{r}_{1,i}$.

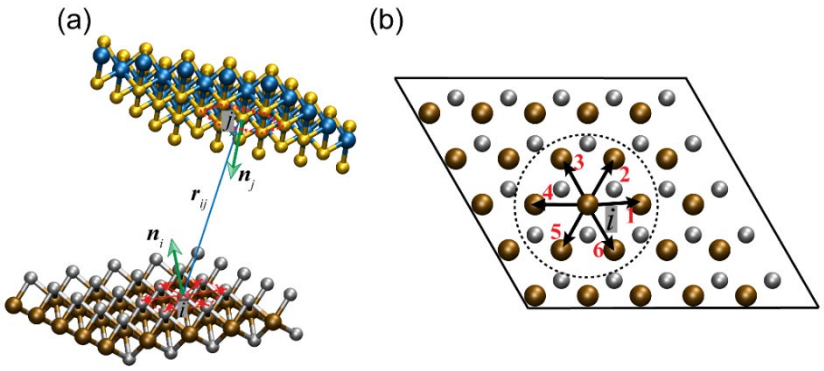

Figure S14. Definition of local normal vectors. For each atom i, its six nearest neighboring atoms within the same sublayer are chosen to define its normal vector $\boldsymbol{n}_i$.

2.5 Protocol for Parameterizing the Force Field

In this section, we provide the protocol for parameterizing the interlayer force field. A set of nine pairwise parameters $\boldsymbol{\xi} = \{\alpha_{ij}, \beta_{ij}, \gamma_{ij}, \varepsilon_{ij}, C_{ij}, d_{ij}, s_{R,ij}, r_{ij}^{\text{eff}}, C_{6,ij}\}$ was obtained by fitting against the $M = M_{\text{b}} + M_{\text{s}}$ (M_{b} and M_{s} denoted the number of BE curves sliding PESs, respectively) reference DFT datasets using the least-square method, where each parameter is symmetric with respect to index interchange due to the symmetry of the interaction. To focus on providing a good description of BE curves in the sub-equilibrium regime and the relatively low energy corrugation of the PESs, we define the following objective function:

$$\Phi(\boldsymbol{\xi}) = \sum_{m=1}^{M_b} w_m^{\text{b}} \left\| E_m^{\text{b}}(\boldsymbol{\xi}) - E_m^{\text{b,DFT}} \right\|_2 + \sum_{m=1}^{M_s} w^{\text{s}} \left\| E_m^{\text{s}}(\boldsymbol{\xi}) - E_m^{\text{s,DFT}} \right\|_2, \tag{S2}$$

where w_m^{b} and w^{s} are weighting factors used for BE curves and sliding PESs, respectively. Here, we set $w_m^{\text{b}}\left(d < d_{\text{eq}}^m\right) = 1$, $w_m^{\text{b}}\left(d \geq d_{\text{eq}}^m\right) = 40$ and $w^{\text{s}} = 100$ to balanced BE curves and PESs. d is the interlayer distance and d_{eq}^m is its equilibrium value for the m^{th} BE curve, and $\|\cdots\|_2$ is the Euclidean 2-norm that measures the difference between the ILP predictions

and the DFT reference data. ILP parameters were optimized by minimizing this objective function using an interior-point algorithm implemented in the MATLAB software suite.

2.6 Interlayer Potential Parameters, Equilibrium Interlayer Distanc , and Binding Energy

In this work, all reference data, including BE curves and sliding potential energy surfaces (PESs), were obtained using PBE+MBD-NL. The ILP parameter values obtained by the fitting procedure described in the main text against DFT reference datasets for the various interfaces considered are presented in **Table S1**. The value of $R_{\mathrm{cut}} = 16\,\text{Å}$ remains consistent across these sets.

Table S1. List of ILP parameters values for laterally periodic bilayer $MoTe_2$ and WTe_2. The training set includes all PBE+MBD-NL bilayer BE and PES results appearing in **Figures S8-S10**. In this table, the parameters of the same atomic pair (for example, Mo-Te and Te-Mo) are symmetric.

	β_{ij}(Å)	α_{ij}	γ_{ij}(Å)	ε_{ij}(meV)	C_{ij}(meV)	d_{ij}	$s_{R,ij}$	$r_{eff,ij}$(Å)	$C_{6,ij}$(eV·Å^6)
Mo-Mo	5.6098	7.8365	1.3179	5.5565	267.3421	115.7180	2.6924	2.0937	491.8491
W-W	6.1150	10.1497	1.3724	0.6390	207.7690	91.6412	1.3011	3.5531	491.8505
Te-Te	3.4142	7.9876	2.5818	0.9697	250.3381	172.6595	0.5900	3.6183	293.4658
Mo-Te	3.9312	24.9618	19.7544	111.2976	182.7056	188.3731	1.7389	2.5846	242.6863
W-Te	3.9941	23.2878	0.0929	14.0313	197.8072	207.0843	1.5186	3.0085	242.6995

In a previous work, DFT calculations indicate that equilibrium distances for AA′-stacked $MoTe_2$ bilayers ranged from 6.9 Å to 7.5 Å, with BEs ranging from 7.5 meV/atom to 25.7 meV/atom. The PBE+MBD-NL, LDA, and D3-BJ methods exhibit comparable BE with differences around ~3.5%. In contrast, PBE, DF, DF2, optPBE, and optB88 were found to overestimate BEs by ~58.3%, ~67.7%, ~69.8%, ~47.6%, and ~36.2%, respectively, compared to PBE+MBD-NL. Other DFT results in **Table S2** differ from PBE+MBD-NL calculations by less than 25%. Furthermore, available DFT results in literatures show that the equilibrium

distances of AA′-stacked WTe_2 bilayers obtained using PBE+MBD-NL vary from other DFT calculations by 0.1% to 5.5%. For BEs of WTe_2 bilayers, the DFT results obtained using methods like LDA, PBE, D3-BJ, DF, DF2, optPBE, and optB88 have shown overestimations compared to that of PBE+MBD-NL by ~24.2%, ~49.4%, ~31.6%, ~56.8%, ~58.2%, ~32.5%, and ~21.1%, respectively. Interestingly, the BE acquired using the dDsC method closely matches with a mere 0.1% disparity. Additionally, other DFT results of bilayer WTe_2 differ from PBE+MBD-NL calculations by less than 8%. Based on the information presented in **Table S2** and **Figure S13**, we can conclude that the PBE+MBD-NL DFT reference data adeptly aligns with the ILP for bilayer structures across the entire range of interlayer distances examined, encompassing even the sub-equilibrium regime.

Table S2. Equilibrium interlayer distance, d_{eq} (Å), and binding energy, E_b (meV/atom) for $MoTe_2$ and WTe_2, calculated at considered stacking modes using PBE+MBD-NL methods, ILP and DFT data from literatures.

Methods		PBE+MBD-NL		ILP		Reference data			
Stacking modes (Bilayer)			d_{eq}	E_b	d_{eq}	E_b	d_{eq}	E_b	Method	Reference
$MoTe_2$	Anti-Parallel configurations	AA′	7.1	24.8	7.2	23.3	6.9	25.7	LDA	Ref. 5
							7.5	10.3	PBE	
							7.0	20.7	D2	
							7.0	20.3	D3	
							6.9	25.7	D3-BJ	
							7.0	20.0	TS	
							7.0	20.2	TS-iter	
							7.0	19.2	dDsC	
							7.5	8.0	DF	
							7.5	7.5	DF2	
							7.0	20.8	rev-DF2	
							7.3	13.0	optPBE	
							7.1	15.8	optB88	
							7.0	20.5	optB86b	
							7.1	18.8	SCAN	
							6.9	--	LDA	Ref. 6

							7.1	--	optB88	
		AB′	7.4	18.7	7.4	19.0	7.1	--	LDA	
							7.3	--	optB88	
		A′B	7.9	13.4	7.9	12.7	7.7	--	LDA	
							7.8	--	optB88	
	Parallel configurations	AB	7.2	22.6	7.2	23.2	6.9	--	LDA	
							7.1	--	optB88	
		AA	8.0	12.9	8.0	11.4	7.7	--	LDA	
							7.8	--	optB88	
WTe_2	Anti-Parallel configurations	AA′	7.1	24.7	7.2	23.1	6.9	30.7	LDA	Ref. 5
							7.5	12.5	PBE	
							6.9	26.5	D2	
							7.0	26.7	D3	
							6.9	32.5	D3-BJ	
							7.1	22.8	TS	
							7.0	25.0	TS-iter	
							7.0	24.7	dDsC	
							7.5	10.7	DF	
							7.4	10.3	DF2	
							7.0	25.3	rev-DF2	
							7.3	16.7	optPBE	
							7.1	19.5	optB88	
							7.0	25.3	optB86b	
							7.1	23.0	SCAN	
							6.9	--	LDA	
							7.1	--	optB88	
		AB′	7.4	18.2	7.2	18.5	7.1	--	LDA	
							7.3	--	optB88	
		A′B	8.0	13.5	8.0	12.6	7.7	--	LDA	Ref. 6
							7.8	--	optB88	
	Parallel configurations	AB	7.2	22.2	7.2	23.0	7.0	--	LDA	
							7.1	--	optB88	
		AA	8.0	13.1	8.0	11.4	7.8	--	LDA	
							7.8	--	optB88	

Intralayer lattice constants of 3.505 and 3.511 Å are used for $MoTe_2$ and WTe_2, respectively.

3. Fitting for Bulk Modulus

Here, three equations of state (EOS) are used to fit the *P*-*V* curve: the Murnaghan equation (Eq. S3),[7, 8] the Birch-Murnaghan equation (Eq. S4),[9, 10] and the Vinet equation (Eq. S5),[11, 12] which take the following forms:

$$\frac{V}{V_0} = [1 + \frac{B'}{B}P]^{\frac{-1}{B'}}, \tag{S3}$$

$$P = 3B\xi(1+2\xi)^{5/2}\left[1 - \frac{3}{2}(4 - B')\xi\right], \xi = \frac{1}{2}[\left(\frac{V}{V_0}\right)^{-\frac{2}{3}} - 1], \tag{S4}$$

$$P = 3B\frac{(1-X)}{X^2}\exp\left[\frac{3}{2}(B'-1)(1-X)\right], X = \left(\frac{V}{V_0}\right)^{\frac{1}{3}}. \tag{S5}$$

Here, V_0 and V are the unit cell volumes in the absence and presence of external hydrostatic pressure, and B and B' are the bulk modulus and its pressure derivative at zero pressure, respectively. The depiction of the relationship between bulk volume (V) and pressure (P) exhibits variability among the three equations. In particular, the Murnaghan, Birch-Murnaghan, and Vinet equations display linear, polynomial, and exponential dependencies on pressure, respectively, when fitting the pressure-volume (*P*-*V*) curve. The corresponding *P*-*V* curve and the outcomes of fitting are illustrated in **Figure S15**.

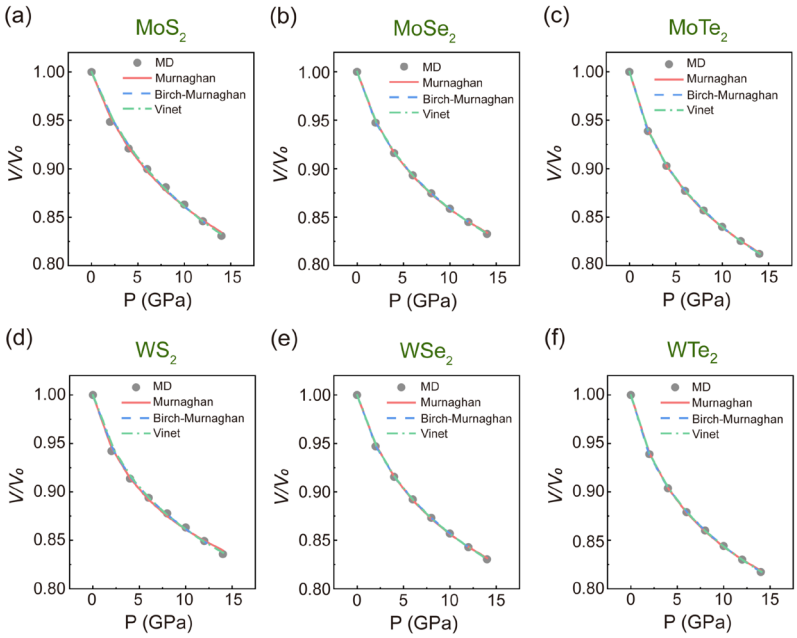

Figure S15. Pressure dependence of the normalized volume V/V_0 of bulk MoS_2 (a), $MoSe_2$ (b), $MoTe_2$ (c), WS_2 (d), WSe_2 (e), and WTe_2 (f). The solid black points are the NPT simulation results. The solid red lines, dashed blue lines, and dashed-dotted green lines are fitted curves generated using Murnaghan, Birch-Murnaghan, and Vinet EOS, respectively.

The results exhibit a high degree of fitting accuracy against the MD simulation reference data, demonstrated by all three EOS. The bulk modulus, B (GPa) and its zero-pressure derivative, B' (GPa) for bulk homojunctions (including MoS_2, $MoSe_2$, $MoTe_2$, WS_2, WSe_2, and WTe_2), are calculated using NEP+ILP force field. Remarkably, there is minimal disparity in the bulk moduli obtained through Murnaghan, Birch-Murnaghan, and Vinet EOS fitting, as shown in **Table S3**.

Table S3. Bulk modulus, B (GPa), and zero-pressure derivative, B' (GPa), of bulk homojunctions (MoS_2, $MoSe_2$, $MoTe_2$, WS_2, WSe_2, and WTe_2), calculated using NEP+ILP force field.

Methods	Murnaghan EOS		Birch−Murnaghan EOS		Vinet EOS	
Stacking modes	B	B'	B	B'	B	B'
MoS_2	35.1 ± 5.8	7.8 ± 1.9	36.2 ± 6.3	8.7 ± 2.8	37.0 ± 5.5	8.1 ± 1.9
$MoSe_2$	29.7 ± 1.6	9.2 ± 0.6	25.9 ± 0.6	14.8 ± 0.5	28.6 ± 1.1	11.1 ± 0.5
$MoTe_2$	24.5 ± 1.0	8.6 ± 0.4	20.9 ± 0.5	14.0 ± 0.4	23.2 ± 0.7	10.6 ± 0.3
WS_2	25.9 ± 4.2	11.2 ± 1.8	22.7 ± 5.8	19.2 ± 7.0	27.3 ± 4.7	12.3 ± 2.3
WSe_2	29.8 ± 1.6	9.0 ± 0.6	26.4 ± 0.7	13.8 ± 0.6	28.8 ± 1.1	10.7 ± 0.5
WTe_2	23.8 ± 1.1	9.4 ± 0.5	19.2 ± 1.0	17.2 ± 1.3	22.5 ± 1.1	11.6 ± 0.5

4. Interlayer Registry Index of Homogeneous $MoTe_2$ and WTe_2

The Registry Index (RI)[13, 14] approach offers an intuitive and computationally efficient geometric measure for quantifying interlayer registry in rigid layered material interfaces, both globally (GRI) and spatially resolved at the local scale (LRI), as they undergo relative sliding. For a TMD interface consisting of two layers, marked as *a* and *b*, and the chemical compositions are marked by $M^aX_2^a$ and $M^bX_2^b$, where $M^{a/b}$ = Mo or W and $X^{a/b}$ = S, Se or Te, the local registry index is calculated as LRI = $f(h_{in}) \times \frac{2\pi\left(\sigma_{t_i}^{t_n}\right)^2\left(\sigma_{t_n}^{t_i}\right)^2}{\left(\sigma_{t_i}^{t_n}\right)^2+\left(\sigma_{t_n}^{t_i}\right)^2} e^{-\frac{d_{in}^2}{2\left(\sigma_{t_i}^{t_n}\right)^2+2\left(\sigma_{t_n}^{t_i}\right)^2}}$, where $\sigma_{t_i}^{t_n}$ represents the effective radius of atoms of type t_i in one layer when interacting with an atom of type t_n in its adjacent layer. d_{in} is the lateral distance between the two atoms and $f(h_{in}) = \exp[-a(h_{in} - h_{in}^0)]$ is a dimensionless scaling factor, used to describe the dependence of the repulsive interaction on vertical interatomic distance h_{in}. Here, a is a fitting parameter and h_{in}^0 is set to the interlayer (vertical) distance between atoms *i* and *n* at the optimal stacking mode.

Previous studies have extended the RI approach to quantify the interlayer commensurability of both homogeneous and heterogeneous interfaces in MoS_2, WS_2, $MoSe_2$, and WSe_2.[13, 14] However, the RI parameterization for $MoTe_2$ and WTe_2 has remained unavailable. In this work, we successfully extend the RI framework to homogeneous $MoTe_2$ and WTe_2 structures. **Figure S16** and **Figure S17** demonstrate excellent agreement between the reference DFT calculations and the GRI predictions for $MoTe_2$ and WTe_2, further validating the approach. Here, the RI effective radii are independently fitted for the parallel and antiparallel stacking configurations, yielding the following values in **Table S4**.

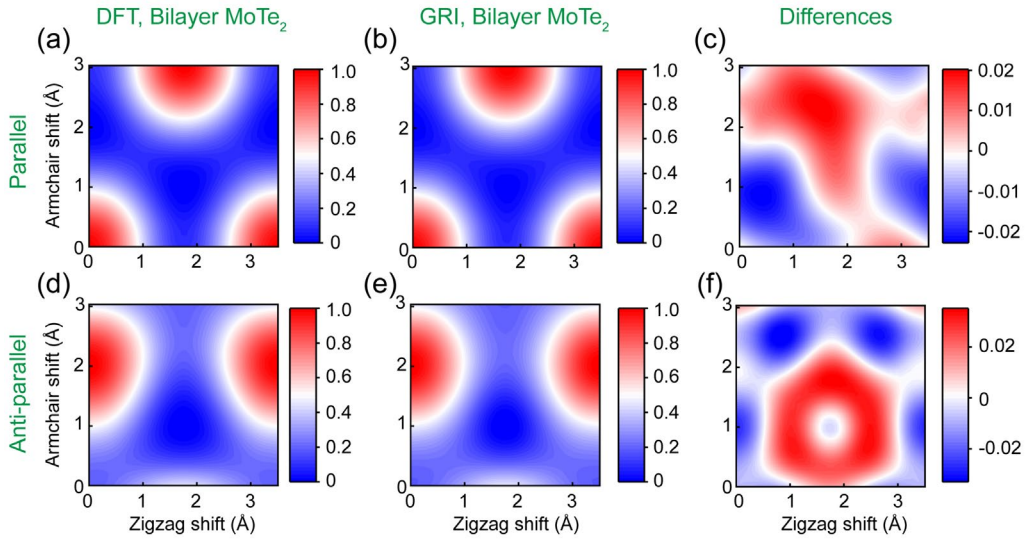

Figure S16. Two-dimensional potential energy surfaces (PESs) of bilayer $MoTe_2$ stacked in the parallel (top) or antiparallel (bottom) orientations calculated using DFT (left column) and the GRI (middle column) under rigid shifts along the armchair and zigzag directions. The energy origins of the DFT PESs obtained for the P and AP orientations are set to the total energies calculated at the same level of theory for the optimal AB and AA′ stacking modes at an interlayer distance of 7.1 Å, respectively, and the PESs are normalized by the energy of the worst AA and A′B stacking modes for P and AP interlayer orientations, respectively. The right panels show the difference between the normalized DFT PESs and the corresponding GRI landscapes. Color bars appear to the right of each panel.

Table S4. Fitted GRI parameters for homogeneous $MoTe_2$ and WTe_2 bilayers. The effective radius of each atom pair appearing in the table is given in units of the $\frac{t}{\sqrt{3}}$, where t is the lattice constant (3.505 Å and 3.511 Å are used for $MoTe_2$ and WTe_2, respectively). P and AP stand for the parallel and antiparallel interlayer orientations.

Orientation		$\sigma_{\mathrm{Mo}}^{\mathrm{Mo}}$	$\sigma_{\mathrm{Mo}}^{\mathrm{Te}}/\sigma_{\mathrm{Te}}^{\mathrm{Mo}}$	$\sigma_{\mathrm{Te}}^{\mathrm{Te}}$	α
$MoTe_2$	P	0.10	0.04	0.31	1.50
	AP	0.10	0.18	0.27	1.50
Orientation		$\sigma_{\mathrm{W}}^{\mathrm{W}}$	$\sigma_{\mathrm{W}}^{\mathrm{Te}}/\sigma_{\mathrm{Te}}^{\mathrm{W}}$	$\sigma_{\mathrm{Te}}^{\mathrm{Te}}$	α
WTe_2	P	0.10	0.04	0.32	1.50
	AP	0.10	0.20	0.27	1.50

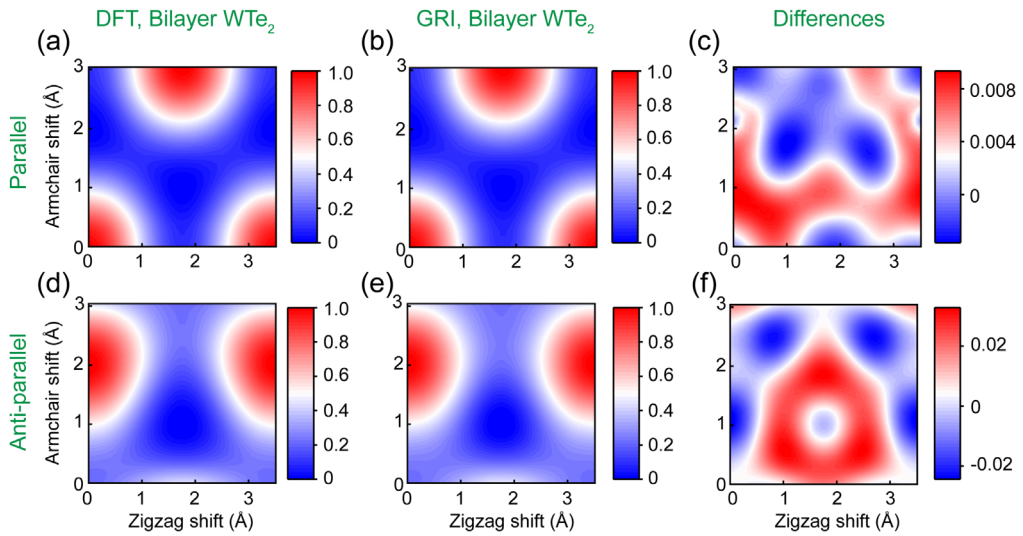

Figure S17. Two-dimensional potential energy surfaces (PESs) of bilayer $MoTe_2$ stacked in the parallel (top) or antiparallel (bottom) orientations calculated using DFT (left column) and the GRI (middle column) under rigid shifts along the armchair and zigzag directions. The energy origins of the DFT PESs obtained for the P and AP orientations are set to the total energies calculated at the same level of theory for the optimal AB and AA′ stacking modes at an interlayer distance of 7.1 Å, respectively, and the PESs are normalized by the energy of the worst AA and A′B stacking modes for P and AP interlayer orientations, respectively. The right panels show the difference between the normalized DFT PESs and the corresponding GRI landscapes. Color bars appear to the right of each panel.

5. HNEMD Simulations

In the homogeneous nonequilibrium molecular dynamics (HNEMD) simulations, we first equilibrated for 200 ps in the isothermal-isobaric (NPT) ensemble at 300K and zero pressure, followed by a 20 ns production stage in the NVT ensemble. The NPT ensemble was maintained by the Berendsen method. The NVT ensemble was maintained by the Nose−Hoover chain thermostat. The external driving force was added during the production stage. Each HNEMD simulation was carried out for up to 20 ns, and the thermal conductivity was well-sampled within steady-state conditions. For each thermal conductivity calculation, we performed three independent simulations and calculated a suitable estimate of statistical error. The size of TMD system and the value of driving force parameter F_e are given in **Table S5**.

Table S5. The size and the value of driving force parameter using HNEMD simulations of monolayer, bilayer, and bulk homojunctions (MoS_2, $MoSe_2$, $MoTe_2$, WS_2, WSe_2, and WTe_2).

	TMDs system	MoS_2	$MoSe_2$	$MoTe_2$	WS_2	WSe_2	WTe_2
Monolayer (κ_{IP})	In-plane Size (nm^2)	638.00	638.92	636.87	639.55	639.23	636.87
	Numbers of atoms	21804	20064	17466	21804	20064	17466
	F_e ($Å^{-1}$)	1×10^{-5}	1×10^{-5}	1×10^{-5}	1×10^{-5}	8×10^{-6}	8×10^{-6}
Bilayer (κ_{IP})	In-plane Size (nm^2)	638.00	638.92	636.87	639.55	639.23	636.87
	Numbers of atoms	43608	40128	34932	43608	40128	34932
	F_e ($Å^{-1}$)	9×10^{-6}	1×10^{-5}	1×10^{-5}	9×10^{-6}	8×10^{-6}	1×10^{-5}
Bulk (κ_{CP})	Size (nm^3)	318.01	365.60	453.66	323.75	370.80	453.66
	Numbers of atoms	17280	17280	17280	17280	17280	17280
	F_e ($Å^{-1}$)	7.5×10^{-6}	7.5×10^{-6}	7.5×10^{-6}	7.5×10^{-6}	7.5×10^{-6}	7.5×10^{-6}

Figure S18 and **Figure S19** show the accumulated averages of the in-plane thermal conductivity for six monolayer and bilayer TMDs (MoS_2, $MoSe_2$, $MoTe_2$, WS_2, WSe_2, and WTe_2) at 300 K and zero pressure. The simulations were conducted on square systems with dimensions of 25 nm × 25 nm, comprising 21804 atoms for monolayer configurations and 43608 atoms for bilayer configurations.

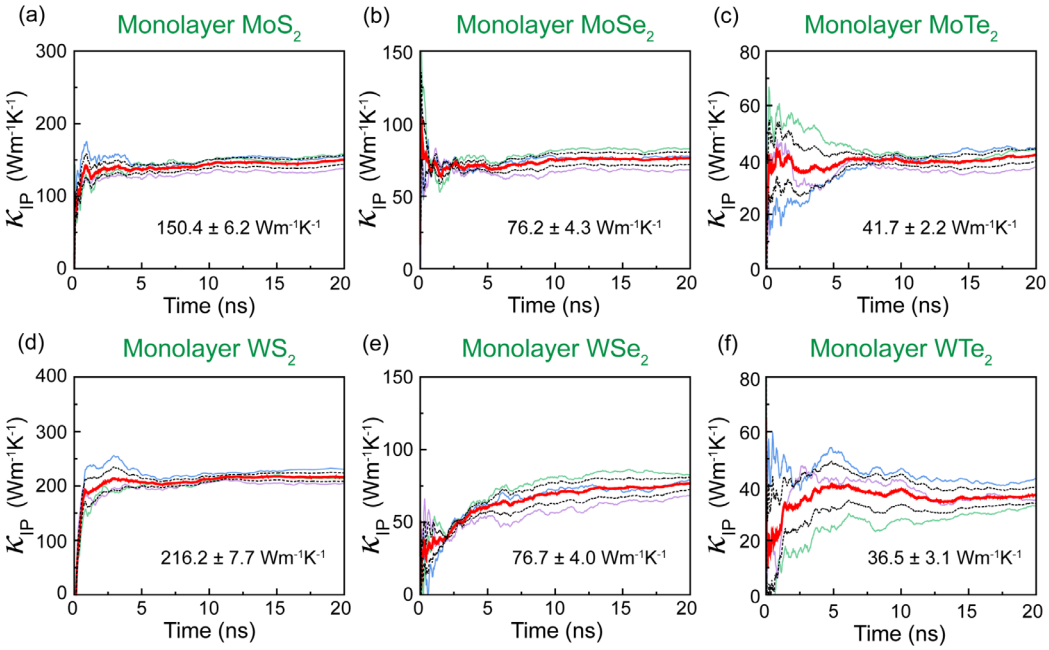

Figure S18. Cumulative average of the in-plane thermal conductivity κ_{IP} for monolayer MoS_2 (a), $MoSe_2$ (b), $MoTe_2$ (c), WS_2 (d), WSe_2 (e), and WTe_2 (f) as a function of the HNEMD production time. In each panel, the thin transparent lines are from three independent runs, and the red solid and black dashed lines represent the average and error bounds from the individual runs.

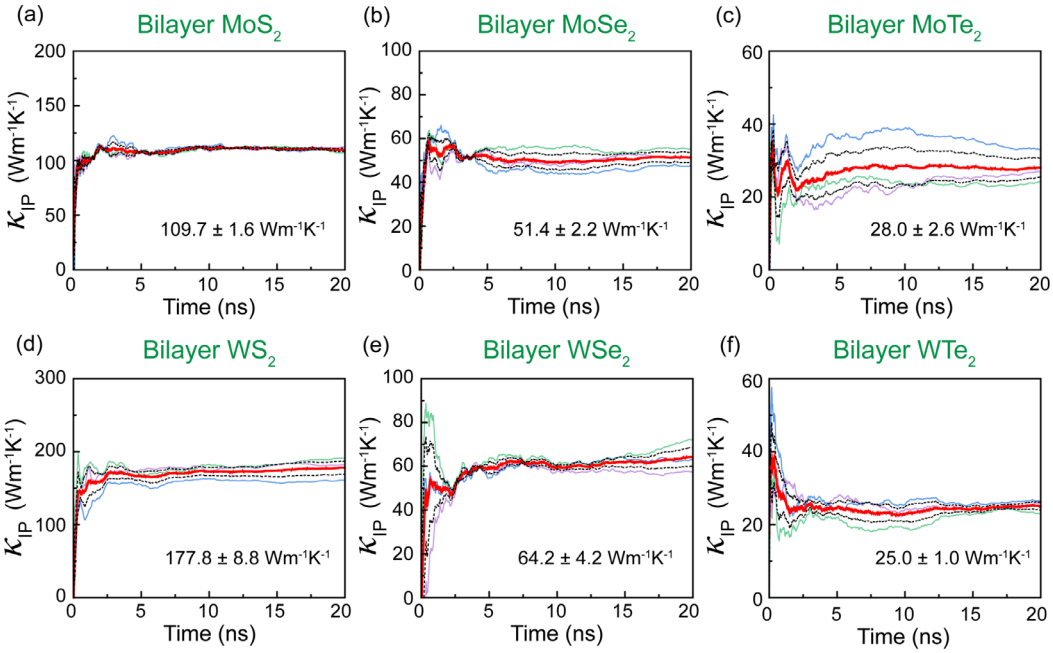

Figure S19. Cumulative average of the in-plane thermal conductivity κ_{IP} for bilayer MoS_2 (a), $MoSe_2$ (b), $MoTe_2$ (c), WS_2 (d), WSe_2 (e), and WTe_2 (f) as a function of the HNEMD production time. In each panel, the thin transparent lines are from three independent runs, and the red solid and black dashed lines represent the average and error bounds from the individual runs.

Figure S20 presents the accumulated averages of the cross-plane thermal conductivity for six bulk TMDs (MoS_2, $MoSe_2$, $MoTe_2$, WS_2, WSe_2, and WTe_2) at 300 K and zero pressure. The simulations were conducted on a 20-layer square bulk system comprising a total of 17280 atoms, with each layer measuring 5 nm × 5 nm. **Figure S21** presents the accumulated averages of the in-plane and cross-plane thermal conductivity for monolayer, bilayer, and bulk MoS_2 at 300 K and zero pressure using NEP-D3 potential. Both κ_{IP} and κ_{CP} have converged with respect to the production time (20 ns).

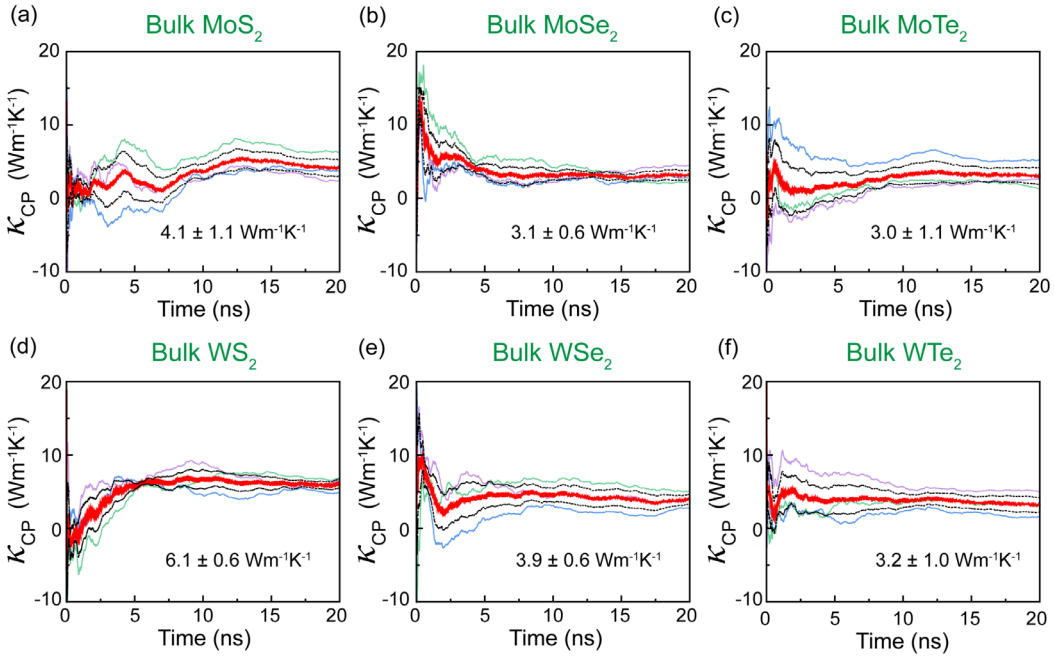

Figure S20. Cumulative average of the cross-plane thermal conductivity κ_{CP} for bulk MoS_2 (a), $MoSe_2$ (b), $MoTe_2$ (c), WS_2 (d), WSe_2 (e), and WTe_2 (f) as a function of the HNEMD production time. In each panel, the thin transparent lines are from three independent runs, and the red solid and black dashed lines represent the average and error bounds from the individual runs.

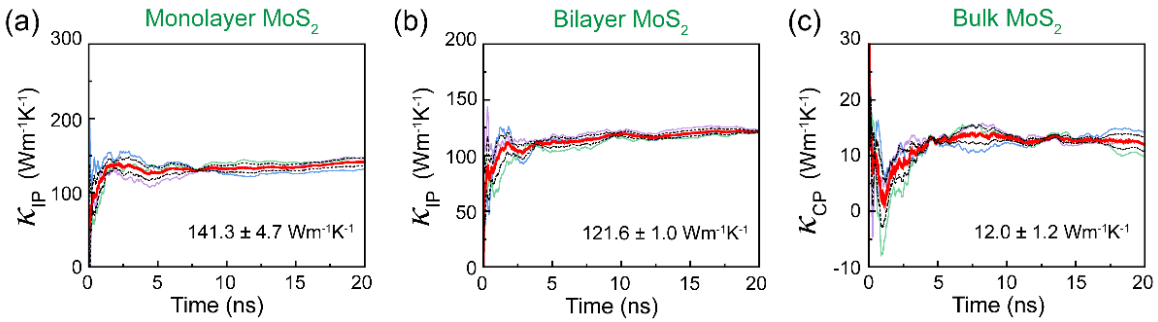

Figure S21. Cumulative average of the in-plane thermal conductivity κ_{IP} for monolayer (a) and bilayer (b) MoS_2 and the cross-plane thermal conductivity κ_{CP} for bulk (c) MoS_2 as a function of the HNEMD production time. In each panel, the thin transparent lines are from three independent runs, and the red solid and black dashed lines represent the average and error bounds from the individual runs.

6. In-plane and Cross-plane Thermal Conductivity of TMDs

As shown in **Table S6**, **Table S7** and **Table S8**, we summarize the converged in-plane and cross-plane thermal conductivity values for the six monolayer, bilayer, and bulk TMDs obtained from the HNEMD method, together with predicted values reported in the literature obtained using experiment (raman spectroscopy, optothermal raman technique, suspended microelectrodes, time-domain thermoreflectance, and steady-state method) and calculated (nonequilibrium Green's function, the Green Kubo, nonequilibrium molecular dynamics, homogeneous nonequilibrium molecular dynamics, equilibrium molecular dynamics, the Peierls-Boltzmann equation and the semiempirical Slack equation) methods.

Table S6. Literature values for theoretical predictions and experiments of in-plane thermal conductivity κ_{IP} in monolayer TMDs (MoS_2, $MoSe_2$, $MoTe_2$, WS_2, WSe_2, and WTe_2) at room temperature, specifying the method used in each calculation and experiment. Nonequilibrium Green's function (NEGF), Green Kubo (GK), nonequilibrium molecular dynamics (NEMD), homogeneous nonequilibrium molecular dynamics (HNEMD), the equilibrium molecular dynamics (EMD), DFT results either in the Peierls-Boltzmann (BTE) method or the semiempirical Slack approach. MD simulations bashed on the Stillinger–Weber empirical potentials (SW), the reactive empirical bond-order potential (REBO), the neuroevolution potential (NEP), Lennard-Jones potential (LJ), the Kolmogorov–Crespi potential (KC) and the interlayer potential (ILP).

Layers	TMD	Method	κ_{IP} ($Wm^{-1}K^{-1}$)	Reference	
Monolayer	MoS_2	Raman Spectroscopy	34.5 ± 4	Yan et al.	Ref. 15
	MoS_2	Raman Spectroscopy	62.2	Taube et al.	Ref. 16
	MoS_2	Optothermal Raman Technique	84 ± 17	Zhang et al.	Ref. 17
	MoS_2	Raman Spectroscopy	19.8	Dolleman et al.	Ref. 18
	MoS_2	Raman spectroscopy	13.3 ± 1.4	Bae et al.	Ref. 19
	MoS_2	Suspended Microelectrodes	24–100	Yang et al.	Ref. 20
	MoS_2	Time-domain Thermoreflectance	82	Jiang et al.	Ref. 21
	MoS_2	NEMD (SW)	32.9	Zhang et al.	Ref. 22
	MoS_2	EMD, NEMD, HNEMD (SW)	193–531	Xu et al.	Ref. 23
	MoS_2	NEMD (SW)	33–54	Wang et al.	Ref. 24

MoS_2	NEMD (SW)	19.76	Ding et al.	Ref. 25
MoS_2	NEMD (SW)	89.43	Mobaraki et al.	Ref. 26
MoS_2	NEMD (SW)	~90	Kandemir et al.	Ref. 27
MoS_2	NEGF	23	Cai et al.	Ref. 28
MoS_2	DFT + Slack	33.6	Peng et al.	Ref. 29
MoS_2	DFT + BTE	34.5	Su et al.	Ref. 30
MoS_2	DFT + BTE	~70	Zulfiqar et al.	Ref. 31
MoS_2	DFT + BTE	83	Li et al.	Ref. 32
MoS_2	DFT + BTE	103	Gu et al.	Ref. 33
MoS_2	DFT + BTE	131	Gandi et al.	Ref. 34
MoS_2	DFT + BTE	~400	Cepellotti et al.	Ref. 35
MoS_2	DFT + BTE	32.4	Farris et al.	Ref. 36
MoS2	DFT + BTE	168	Bao et al.	Ref. 37
MoS_2	DFT + BTE	138–155	Gu et al.	Ref. 38
MoS_2	HNMED (NEP)	150.4 ± 6.2	This work	-
$MoSe_2$	Time-domain Thermoreflectance	35	Jiang et al.	Ref. 21
$MoSe_2$	Optothermal Raman Technique	59 ± 18	Zhang et al.	Ref. 17
$MoSe_2$	Optothermal Raman Technique	38 ± 4	Mandal et al.	Ref. 39
$MoSe_2$	NEMD (SW)	24.8	Zhang et al.	Ref. 22
$MoSe_2$	NEMD (SW)	29.05	Mobaraki et al.	Ref. 26
$MoSe_2$	NEMD (SW)	~40	Kandemir et al.	Ref. 27
$MoSe_2$	DFT + Slack	17.6	Peng et al.	Ref. 29
$MoSe_2$	DFT + BTE	~57	Zulfiqar et al.	Ref. 31
$MoSe_2$	DFT + BTE	54	Gu et al.	Ref. 33
$MoSe_2$	DFT + BTE	51.5–70.3	Gupta et al.	Ref. 40
$MoSe_2$	DFT + GK	39	Gupta et al.	Ref. 40
$MoSe_2$	DFT + BTE	20.6	Farris et al.	Ref. 36
$MoSe_2$	DFT + BTE	~60	Kumar et al.	Ref. 41
$MoSe_2$	HNMED (NEP)	76.2 ± 4.3	This work	-
$MoTe_2$	DFT + BTE	~46	Zulfiqar et al.	Ref. 31
$MoTe_2$	DFT + BTE	43–49	Kaur et al.	Ref. 42
$MoTe_2$	DFT + BTE	70.86	Shen et al.	Ref. 43
$MoTe_2$	DFT + BTE	43.26–45.84	Zhang et al.	Ref. 44
$MoTe_2$	DFT + BTE	42.2	Shafique et al.	Ref. 45
$MoTe_2$	HNMED (NEP)	41.7 ± 2.2	This work	-
WS_2	Raman Spectroscopy	32	Peimyoo et al.	Ref. 46
WS_2	Time-domain Thermoreflectance	120	Jiang et al.	Ref. 21

WS_2	NEMD (SW)	91.66	Mobaraki et al.	Ref. 26
WS_2	DFT + Slack	31.8	Peng et al.	Ref. 29
WS_2	DFT + BTE	142	Gu et al.	Ref. 33
WS_2	DFT + BTE	42.2	Farris et al.	Ref. 36
WS_2	DFT + BTE	113.97	Zulfiqar et al.	Ref. 31
WS_2	DFT + BTE	262.78	Han et al.	Ref. 47
WS_2	DFT + BTE	212.3	Bao et al.	Ref. 37
WS_2	DFT + BTE	~215	et al.	Ref. 48
WS_2	HNMED (NEP)	216.2 ± 7.7	This work	-
WSe_2	Time-domain Thermoreflectance	42	Jiang et al.	Ref. 21
WSe_2	Raman spectroscopy	37 ± 12	Easy et al.	Ref. 49
WSe_2	Raman spectroscopy	49 ± 14	Easy et al.	Ref. 49
WSe_2	DFT + BTE	~39	Zulfiqar et al.	Ref. 31
WSe_2	DFT + BTE	~32	Kumar et al.	Ref. 41
WSe_2	DFT + BTE	~120	Zhang et al.	Ref. 48
WSe_2	HNMED (NEP)	76.7 ± 4.0	This work	-
WTe_2	DFT + BTE	33.66	Zulfiqar et al.	Ref. 31
WTe_2	DFT + BTE	74.69	Shen et al.	Ref. 43
WTe_2	DFT + BTE	~40	Zhang et al.	Ref. 48
WTe_2	HNMED (NEP)	36.5 ± 3.1	This work	-

Table S7. Literature values for theoretical predictions and experiments of in-plane thermal conductivity κ_{IP} in bilayer TMDs (MoS_2, $MoSe_2$, $MoTe_2$, WS_2, WSe_2, and WTe_2) at room temperature, specifying the method used in each calculation and experiment.

Layers	TMD	Method	κ_{IP} ($Wm^{-1}K^{-1}$)	Reference	
Bilayer	MoS_2	Optothermal Raman Technique	77 ± 25	Zhang et al.	Ref. 17
	MoS_2	Raman spectroscopy	15.6 ± 1.5	Bae et al.	Ref. 19
	MoS_2	NEMD (SW+KC)	75.63	Mandal et al.	Ref. 50
	MoS_2	NEMD (REBO+ILP)	15.1 ± 1.2	Jiang et al.	Ref. 51
	MoS_2	NEMD (SW+ILP)	40.7 ± 1.6	Jiang et al.	Ref. 51
	MoS_2	DFT + BTE	108–125	Gu et al.	Ref. 38
	MoS_2	DFT + BTE	199.3	Bao et al.	Ref. 37
	MoS_2	HNMED (NEP+ILP)	109.7 ± 1.6	This work	-
	$MoSe_2$	Optothermal Raman Technique	42 ± 13	Zhang et al.	Ref. 17
	$MoSe_2$	DFT + BTE	~21	Li et al.	Ref. 52
	$MoSe_2$	HNMED (NEP+ILP)	51.4 ± 2.2	This work	-
	$MoTe_2$	HNMED (NEP+ILP)	28.0 ± 2.6	This work	-
	WS_2	Raman Spectroscopy	53	Peimyoo et al.	Ref. 46
	WS_2	Steady-state Method	124	Pisoni et al.	Ref. 53
	WS_2	DFT + BTE	269.2	Bao et al.	Ref. 37
	WS_2	HNMED (NEP+ILP)	177.8 ± 8.8	This work	-
	WSe_2	Raman spectroscopy	24 ± 12	Easy et al.	Ref. 49
	WSe_2	DFT + BTE	70.91–78.38	Luo et al.	Ref. 54
	WSe_2	HNMED (NEP+ILP)	64.2 ± 4.2	This work	-
	WTe_2	DFT + BTE	55.05–59.97	Luo et al.	Ref. 54
	WTe_2	HNMED (NEP+ILP)	25.0 ± 1.0	This work	-

Table S8. Literature values for theoretical predictions and experiments of cross-plane thermal conductivity κ_{CP} in bulk TMDs (MoS_2, $MoSe_2$, $MoTe_2$, WS_2, WSe_2, and WTe_2) at room temperature, specifying the method used in each calculation and experiment.

Layer	TMD	Method	κ_{CP} ($Wm^{-1}K^{-1}$)	Reference	
Bulk	MoS_2	Pump-probe Metrology	2.0 ± 0.3	Liu et al.	Ref. 55
	MoS_2	Time-domain Thermoreflectance	~2.3	Muratore et al.	Ref. 56
	MoS_2	Time-domain Thermoreflectance	0.9–2.0	Sood et al.	Ref. 57
	MoS_2	Time-domain Thermoreflectance	2.0	Zhu et al.	Ref. 58
	MoS_2	Time-domain Thermoreflectance	4.75 ± 0.32	Jiang et al.	Ref. 21
	MoS_2	HNEMD (bond-order potential)	3.7 ± 0.5	Kim et al.	Ref. 59
	MoS_2	NEMD (REBO + ILP)	~0.24	Jiang et al.	Ref. 51
	MoS_2	NEMD (SW + ILP)	~0.47	Jiang et al.	Ref. 51
	MoS_2	HNEMD (REBP + LJ)	2.0 ± 0.2	Xu et al.	Ref. 23
	MoS_2	EMD (NEP)	~4	Eriksson et al.	Ref. 60
	MoS_2	DFT + BTE	~5	Sood et al.	Ref. 57
	MoS_2	DFT + BTE	5.1	Lindroth et al.	Ref. 61
	MoS_2	HNEMD (NEP + ILP)	4.1 ± 1.1	This work	-
	$MoSe_2$	Time-domain Thermoreflectance	~2.8	Jiang et al.	Ref. 21
	$MoSe_2$	DFT + BTE	~3.6	Lindroth et al.	Ref. 61
	$MoSe_2$	HNEMD (NEP + ILP)	3.10 ± 0.6	This work	-
	$MoTe_2$	Time-domain Thermoreflectance	~1.4	Yan et al.	Ref. 62
	$MoTe_2$	DFT + BTE	2.5	Li et al.	Ref. 63
	$MoTe_2$	DFT + BTE	~2.9	Lindroth et al.	Ref. 61
	$MoTe_2$	HNEMD (NEP + ILP)	3.0 ± 1.1	This work	-
	WS_2	Time-domain Thermoreflectance	~3	Jiang et al.	Ref. 21
	WS_2	DFT + BTE	4.7	Lindroth et al.	Ref. 61
	WS_2	HNEMD (NEP + ILP)	6.1 ± 0.6	This work	-
	WSe_2	Time-domain Thermoreflectance	~1.3	Muratore et al.	Ref. 56
	WSe_2	Time-domain Thermoreflectance	~2.4	Jiang et al.	Ref. 21
	WSe_2	DFT + BTE	3.0	Lindroth et al.	Ref. 61
	WSe_2	HNEMD (NEP + ILP)	3.9 ± 0.6	This work	-
	WTe_2	DFT + BTE	2.8	Lindroth et al.	Ref. 61
	WTe_2	HNEMD (NEP + ILP)	3.2 ± 1.0	This work	-

7. Binding and Sliding Energy of Bilayer MoS_2 Calculated Using Different DFT Methods

In the main text, we observed that the binding energy and sliding energy barriers calculated using NEP-D3 are approximately twice as large as those obtained from HSE+MBD-NL and NEP+ILP. To elucidate the source of this discrepancy, we conducted a more detailed analysis of the differences in binding energy and sliding energy of bilayer MoS_2 as calculated by various DFT methods (PBE+D3, PBE+MBD, PBE+MBD-NL, and HSE+MBD-NL).

Figure S22a shows the equilibrium interlayer distances of bilayer MoS_2 calculated using four different DFT methods as 6.1 Å (PBE+D3), 6.1 Å (PBE+MBD), 6.3 Å (PBE+MBD-NL), and 6.2 Å (HSE+MBD-NL), with the corresponding binding energies at these equilibrium distances being -44.99 meV/atom (PBE+D3), -30.67meV/atom(PBE+MBD), -19.23 meV/atom (PBE+MBD-NL), and -21.02 meV/atom (HSE+MBD-NL), respectively. Therefore, the significant differences shown in the main text arise because NEP-D3 and NEP+ILP use D3 and MBD-NL, respectively, to describe the interlayer van der Waals interactions. Additionally, the sliding energy at the equilibrium interlayer distance illustrated in **Figure S22**b further highlights the differences between the four DFT methods, with PBE+D3 yielding significantly higher values compared to HSE+MBD-NL.

Figure S23 presents the sliding potential energy surfaces (PES) calculated using NEP-D3 and NEP+ILP at interlayer distances of 6.0 Å and 6.2 Å, respectively. The sliding PES predicted by NEP-D3 exhibits distinct energy landscapes at different interlayer distances (see **Figures S23**a,b), which can be attributed to the absence of sliding configurations at 6.2 Å in the training dataset, thereby limiting its transferability. To improve the accuracy of NEP-D3 in describing the sliding energy landscape at 6.2 Å, additional training data incorporating sliding configurations at this interlayer distance would be required. In contrast, NEP+ILP demonstrates superior generalizability (see **Figures S23**c,d), making it a more reliable approach for studying interfacial interactions in layered materials.

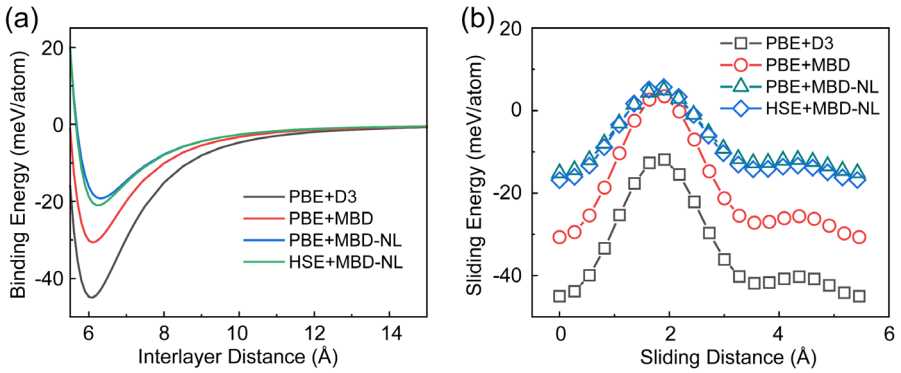

Figure S22. (a) Binding energy curves of the laterally periodic structures of bilayer MoS_2 calculated using PBE+D3 (black line), PBE+MBD (red line), PBE+MBD-NL (blue line), and HSE+MBD-NL (green line) methods. The reported energies are measured relative to the value obtained for infinitely separated layers. (b) Sliding energies along the AA′-A′B-AB′-SP path of bilayer MoS_2 with the equilibrium interlayer distance computed from various PBE+D3 (black rectangle), PBE+MBD (red circle), PBE+MBD-NL (green triangle), and HSE+MBD-NL (blue diamond) methods. All the energies are normalized by the total number of atoms in the unit cell (6 atoms).

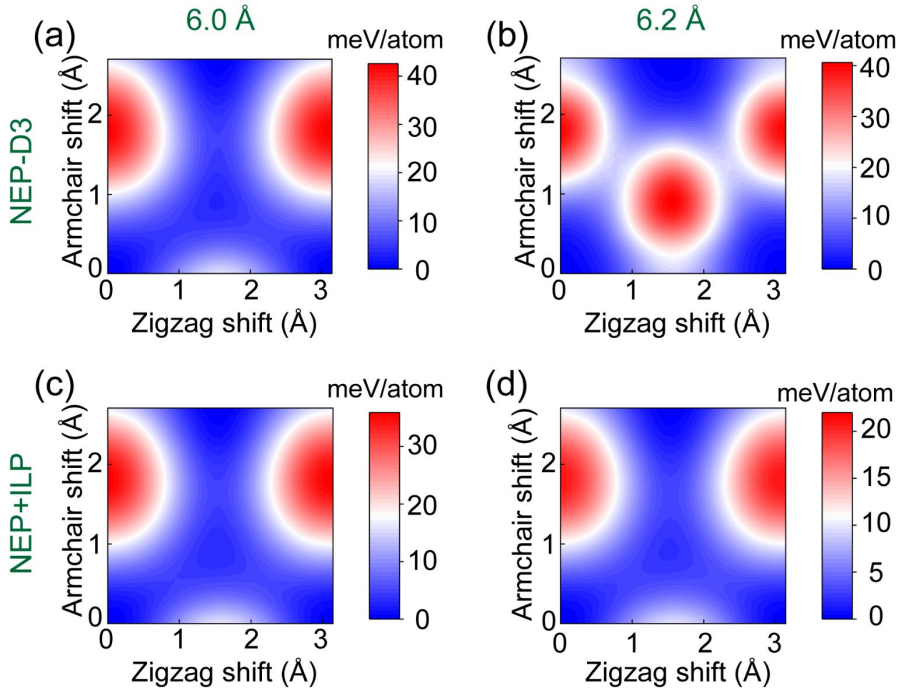

Figure S23. Sliding PESs of the laterally periodic bilayer MoS_2, calculated at an interlayer distance of 6.0 Å (a,c) and 6.2 Å (b,d) for top panels (using NEP-D3 method) and bottom panels (using NEP+ILP method). All the energies are normalized by the total number of atoms in the unit cell (6 atoms).

References

(1) Fan, Z.; Wang, Y.; Ying, P.; Song, K.; Wang, J.; Wang, Y.; Zeng, Z.; Xu, K.; Lindgren, E.; Rahm, J. M.; Gabourie, A. J.; Liu, J.; Dong, H.; Wu, J.; Chen, Y.; Zhong, Z.; Sun, J.; Erhart, P.; Su, Y.; Ala-Nissila, T., GPUMD: A package for constructing accurate machine-learned potentials and performing highly efficient atomistic simulations. *J. Chem. Phys.* **2022,** *157* (11), 114801.
(2) Jiang, W.; Sofer, R.; Gao, X.; Tkatchenko, A.; Kronik, L.; Ouyang, W.; Urbakh, M.; Hod, O., Anisotropic Interlayer Force Field for Group-VI Transition Metal Dichalcogenides. *J. Phys. Chem. A* **2023,** *127* (46), 9820-9830.
(3) Hermann, J.; Tkatchenko, A., Density Functional Model for van der Waals Interactions: Unifying Many-Body Atomic Approaches with Nonlocal Functionals. *Phys. Rev. Lett.* **2020,** *124* (14), 146401.
(4) Blum, V.; Gehrke, R.; Hanke, F.; Havu, P.; Havu, V.; Ren, X.; Reuter, K.; Scheffler, M., Ab initio molecular simulations with numeric atom-centered orbitals. *Comput. Phys. Commun.* **2009,** *180* (11), 2175-2196.
(5) Pisarra, M.; Díaz, C.; Martín, F., Theoretical study of structural and electronic properties of 2H-phase transition metal dichalcogenides. *Phys. Rev. B* **2021,** *103* (19), 195416.
(6) Zeng, F.; Zhang, W.-B.; Tang, B.-Y., Electronic structures and elastic properties of monolayer and bilayer transition metal dichalcogenides MX_2 (M = Mo, W; X = O, S, Se, Te): A comparative first-principles study. *Chin. Phys. B* **2015,** *24* (9), 097103.
(7) Murnaghan, F. D., The Compressibility of Media under Extreme Pressures. *Proc. Natl. Acad. Sci. U.S.A.* **1944,** *30* (9), 244-247.
(8) Hanfland, M.; Beister, H.; Syassen, K., Graphite under pressure: Equation of state and first-order Raman modes. *Phys. Rev. B Condens. Matter.* **1989,** *39* (17), 12598-12603.
(9) Birch, F., Finite Elastic Strain of Cubic Crystals. *Phys. Rev.* **1947,** *71* (11), 809-824.
(10) Birch, F., Elasticity and constitution of the Earth's interior. *J. Geophys. Res.* **1952,** *57* (2), 227-286.
(11) Vinet, P.; Ferrante, J.; Smith, J. R.; Rose, J. H., A universal equation of state for solids. *J. Phys. C: Solid State Phys.* **1986,** *19*, L467-L473.
(12) Vinet, P.; Smith, J. R.; Ferrante, J.; Rose, J. H., Temperature effects on the universal equation of state of solids. *Phys. Rev. B Condens. Matter.* **1987,** *35* (4), 1945-1953.
(13) Hod, O., The registry index: a quantitative measure of materials' interfacial commensurability. *Chemphyschem* **2013,** *14* (11), 2376-91.
(14) Cao, W.; Hod, O.; Urbakh, M., Interlayer Registry Index of Layered Transition Metal Dichalcogenides. *J Phys. Chem. Lett.* **2022,** *13* (15), 3353-3359.
(15) Yan, R.; Simpson, J. R.; Bertolazzi, S.; Brivio, J.; Watson, M.; Wu, X.; Kis, A.; Luo, T.; Hight Walker, A. R.; Xing, H. G., Thermal Conductivity of Monolayer Molybdenum Disulfide Obtained from Temperature-Dependent Raman Spectroscopy. *ACS Nano* **2014,** *8* (1), 986-993.
(16) Taube, A.; Judek, J.; Łapińska, A.; Zdrojek, M., Temperature-Dependent Thermal Properties of Supported MoS_2 Monolayers. *ACS Appl. Mater. Interfaces* **2015,** *7* (9), 5061-5065.
(17) Zhang, X.; Sun, D.; Li, Y.; Lee, G.-H.; Cui, X.; Chenet, D.; You, Y.; Heinz, T. F.; Hone, J. C., Measurement of Lateral and Interfacial Thermal Conductivity of Single- and Bilayer MoS_2 and $MoSe_2$ Using Refined Optothermal Raman Technique. *ACS Appl. Mater. Interfaces* **2015,**

7 (46), 25923-25929.
(18) Dolleman, R. J.; Lloyd, D.; Lee, M.; Bunch, J. S.; van der Zant, H. S. J.; Steeneken, P. G., Transient thermal characterization of suspended monolayer MoS_2. *Phys. Rev. Mater.* **2018,** *2* (11), 114008.
(19) Bae, J. J.; Jeong, H. Y.; Han, G. H.; Kim, J.; Kim, H.; Kim, M. S.; Moon, B. H.; Lim, S. C.; Lee, Y. H., Thickness-dependent in-plane thermal conductivity of suspended MoS_2 grown by chemical vapor deposition. *Nanoscale* **2017,** *9* (7), 2541-2547.
(20) Yang, X.; Zheng, X.; Liu, Q.; Zhang, T.; Bai, Y.; Yang, Z.; Chen, H.; Liu, M., Experimental Study on Thermal Conductivity and Rectification in Suspended Monolayer MoS_2. *ACS Appl. Mater. Interfaces* **2020,** *12* (25), 28306-28312.
(21) Jiang, P.; Qian, X.; Gu, X.; Yang, R., Probing Anisotropic Thermal Conductivity of Transition Metal Dichalcogenides MX_2 (M = Mo, W and X = S, Se) using Time-Domain Thermoreflectance. *Adv. Mater.* **2017,** *29* (36), 1701068.
(22) Zhang, J.; Hong, Y.; Wang, X.; Yue, Y.; Xie, D.; Jiang, J.; Xiong, Y.; Li, P., Phonon Thermal Properties of Transition-Metal Dichalcogenides MoS_2 and $MoSe_2$ Heterostructure. *J. Phys. Chem. C* **2017,** *121* (19), 10336-10344.
(23) Xu, K.; Gabourie, A. J.; Hashemi, A.; Fan, Z.; Wei, N.; Farimani, A. B.; Komsa, H.-P.; Krasheninnikov, A. V.; Pop, E.; Ala-Nissila, T., Thermal transport in MoS_2 from molecular dynamics using different empirical potentials. *Phys. Rev. B* **2019,** *99* (5), 054303.
(24) Wang, X.; Tabarraei, A., Phonon thermal conductivity of monolayer MoS_2. *Appl. Phys. Lett.* **2016,** *108* (19), 191905.
(25) Ding, Z.; Jiang, J.-W.; Pei, Q.-X.; Zhang, Y.-W., In-plane and cross-plane thermal conductivities of molybdenum disulfide. *Nanotechnology* **2015,** *26* (6), 065703.
(26) Mobaraki, A.; Sevik, C.; Yapicioglu, H.; Çakır, D.; Gülseren, O., Temperature-dependent phonon spectrum of transition metal dichalcogenides calculated from the spectral energy density: Lattice thermal conductivity as an application. *Phys. Rev. B* **2019,** *100* (3), 035402.
(27) Kandemir, A.; Yapicioglu, H.; Kinaci, A.; Çağın, T.; Sevik, C., Thermal transport properties of MoS_2 and $MoSe_2$ monolayers. *Nanotechnology* **2016,** *27* (5), 055703.
(28) Cai, Y.; Lan, J.; Zhang, G.; Zhang, Y.-W., Lattice vibrational modes and phonon thermal conductivity of monolayer MoS_2. *Phys. Rev. B* **2014,** *89* (3), 035438.
(29) Peng, B.; Zhang, H.; Shao, H.; Xu, Y.; Zhang, X.; Zhu, H., Thermal conductivity of monolayer MoS_2, $MoSe_2$, and WS_2: interplay of mass effect, interatomic bonding and anharmonicity. *RSC Adv.* **2016,** *6* (7), 5767-5773.
(30) Su, J.; Liu, Z.-t.; Feng, L.-p.; Li, N., Effect of temperature on thermal properties of monolayer MoS_2 sheet. *J. Alloys Compd.* **2015,** *622*, 777-782.
(31) Zulfiqar, M.; Zhao, Y.; Li, G.; Li, Z.; Ni, J., Intrinsic Thermal conductivities of monolayer transition metal dichalcogenides MX_2 (M = Mo, W; X = S, Se, Te). *Sci. Rep.* **2019,** *9* (1), 4571.
(32) Li, W.; Carrete, J.; Mingo, N., Thermal conductivity and phonon linewidths of monolayer MoS_2 from first principles. *Appl. Phys. Lett.* **2013,** *103* (25), 253103.
(33) Gu, X.; Yang, R., Phonon transport in single-layer transition metal dichalcogenides: A first-principles study. *Appl. Phys. Lett.* **2014,** *105* (13), 131903.
(34) Gandi, A. N.; Schwingenschlögl, U., Thermal conductivity of bulk and monolayer MoS_2. *Europhys. Lett.* **2016,** *113* (3), 36002.
(35) Cepellotti, A.; Fugallo, G.; Paulatto, L.; Lazzeri, M.; Mauri, F.; Marzari, N., Phonon

hydrodynamics in two-dimensional materials. *Nat. Commun.* **2015,** *6* (1), 6400.
(36) Farris, R.; Hellman, O.; Zanolli, Z.; Saleta Reig, D.; Varghese, S.; Ordejón, P.; Tielrooij, K.-J.; Verstraete, M. J., Microscopic understanding of the in-plane thermal transport properties of *2H* transition metal dichalcogenides. *Phys. Rev. B* **2024,** *109* (12), 125422.
(37) Bao, W.; Chen, G.; Wang, Z.; Tang, D., Bilateral phonon transport modulation of Bi-layer TMDCs (MX_2, M=Mo, W; X=S). *Int. J. Therm. Sci.* **2022,** *179*, 107669.
(38) Gu, X.; Li, B.; Yang, R., Layer thickness-dependent phonon properties and thermal conductivity of MoS_2. *J. Appl. Phys.* **2016,** *119* (8), 085106.
(39) Mandal, M.; Maity, N.; Barman, P. K.; Srivastava, A.; Singh, A. K.; Nayak, P. K.; Sethupathi, K., Probing angle-dependent thermal conductivity in twisted bilayer $MoSe_2$. *Phys. Rev. B* **2023,** *108* (11), 115439.
(40) Gupta, M. K.; Kumar, S.; Mittal, R.; Mishra, S. K.; Rols, S.; Delaire, O.; Thamizhavel, A.; Sastry, P. U.; Chaplot, S. L., Distinct anharmonic characteristics of phonon-driven lattice thermal conductivity and thermal expansion in bulk $MoSe_2$ and WSe_2. *J. Mater. Chem. A* **2023,** *11* (40), 21864-21873.
(41) Kumar, S.; Schwingenschlögl, U., Thermoelectric Response of Bulk and Monolayer $MoSe_2$ and WSe_2. *Chem. Mater.* **2015,** *27* (4), 1278-1284.
(42) Kaur, B.; Gupta, R.; Dhiman, S.; Kaur, K.; Bera, C., Anisotropic thermoelectric figure of merit in $MoTe_2$ monolayer. *Phys. B* **2023,** *661*, 414898.
(43) Shen, J.; Han, D.; Zhang, B.; Cao, R.; Liu, Y.; Zheng, S.; Li, H.; Jiang, Y.; Xue, Y.; Xue, M., First-principles study on phonon transport properties of $MoTe_2$ and WTe_2 monolayers in different phases. *Phys. E* **2023,** *145*, 115509.
(44) Zhang, D.; Ren, W.; Wang, K.; Chen, S.; Zhang, L.; Ni, Y.; Zhang, G., A thermal conductivity switch via the reversible 2H-1T′ phase transition in monolayer $MoTe_2$. *Chin. Phys. B* **2023,** *32* (5), 050505.
(45) Shafique, A.; Shin, Y.-H., Strain engineering of phonon thermal transport properties in monolayer 2H-$MoTe_2$. *Phys.Chem.Chem.Phys.* **2017,** *19* (47), 32072-32078.
(46) Peimyoo, N.; Shang, J.; Yang, W.; Wang, Y.; Cong, C.; Yu, T., Thermal conductivity determination of suspended mono- and bilayer WS_2 by Raman spectroscopy. *Nano Res.* **2015,** *8* (4), 1210-1221.
(47) Han, D.; Sun, H.; Ding, W.; Chen, Y.; Wang, X.; Cheng, L., Effect of biaxial strain on thermal transport in WS_2 monolayer from first principles calculations. *Phys. E Low-Dimens. Syst. Nanostruct.* **2020,** *124*, 114312.
(48) Zhang, Z.; Xie, Y.; Ouyang, Y.; Chen, Y., A systematic investigation of thermal conductivities of transition metal dichalcogenides. *Int. J. Heat Mass Transf.* **2017,** *108*, 417-422.
(49) Easy, E.; Gao, Y.; Wang, Y.; Yan, D.; Goushehgir, S. M.; Yang, E.-H.; Xu, B.; Zhang, X., Experimental and Computational Investigation of Layer-Dependent Thermal Conductivities and Interfacial Thermal Conductance of One- to Three-Layer WSe_2. *ACS Appl. Mater. Interfaces* **2021,** *13* (11), 13063-13071.
(50) Mandal, S.; Maity, I.; Das, A.; Jain, M.; Maiti, P. K., Tunable lattice thermal conductivity of twisted bilayer MoS_2. *Phys. Chem. Chem. Phys.* **2022,** *24* (22), 13860-13868.
(51) Jiang, W.; Liang, T.; Xu, J.; Ouyang, W., Twist-Dependent Anisotropic Thermal Conductivity in Homogeneous MoS_2 Stacks. *Int. J. Heat Mass Transf.* **2023,** *217*, 124662.

(52) Li, W.; Yang, L.; Yang, K., Tunable lattice thermal conductivity of 2D $MoSe_2$ via biaxial strain: a comparative study between the monolayer and bilayer. *Appl. Phys. A* **2024,** *130* (5), 356.
(53) Pisoni, A.; Jacimovic, J.; Gaál, R.; Náfrádi, B.; Berger, H.; Révay, Z.; Forró, L., Anisotropic transport properties of tungsten disulfide. *Scripta Mater.* **2016,** *114*, 48-50.
(54) Luo, Y.; Lan, J.-Q.; Zhang, T.; Hu, C.-E.; Chen, X.-R.; Geng, H.-Y., Strain dependences of electronic properties, band alignments and thermal properties of bilayer WX_2 (X = Se, Te). *Philos. Mag.* **2022,** *102* (22), 2323-2343.
(55) Liu, J.; Choi, G.-M.; Cahill, D. G., Measurement of the anisotropic thermal conductivity of molybdenum disulfide by the time-resolved magneto-optic Kerr effect. *J. Appl. Phys.* **2014,** *116* (23), 233107.
(56) Muratore, C.; Varshney, V.; Gengler, J. J.; Hu, J. J.; Bultman, J. E.; Smith, T. M.; Shamberger, P. J.; Qiu, B.; Ruan, X.; Roy, A. K.; Voevodin, A. A., Cross-plane thermal properties of transition metal dichalcogenides. *Appl. Phys. Lett.* **2013,** *102* (8), 081604.
(57) Sood, A.; Xiong, F.; Chen, S.; Cheaito, R.; Lian, F.; Asheghi, M.; Cui, Y.; Donadio, D.; Goodson, K. E.; Pop, E., Quasi-Ballistic Thermal Transport Across MoS_2 Thin Films. *Nano Lett.* **2019,** *19* (4), 2434-2442.
(58) Zhu, G.; Liu, J.; Zheng, Q.; Zhang, R.; Li, D.; Banerjee, D.; Cahill, D. G., Tuning thermal conductivity in molybdenum disulfide by electrochemical intercalation. *Nat. Commun.* **2016,** *7* (1), 13211.
(59) Kim, S. E.; Mujid, F.; Rai, A.; Eriksson, F.; Suh, J.; Poddar, P.; Ray, A.; Park, C.; Fransson, E.; Zhong, Y.; Muller, D. A.; Erhart, P.; Cahill, D. G.; Park, J., Extremely anisotropic van der Waals thermal conductors. *Nature* **2021,** *597* (7878), 660-665.
(60) Eriksson, F.; Fransson, E.; Linderälv, C.; Fan, Z.; Erhart, P., Tuning the Through-Plane Lattice Thermal Conductivity in van der Waals Structures through Rotational (Dis)ordering. *ACS Nano* **2023,** *17* (24), 25565-25574.
(61) Lindroth, D. O.; Erhart, P., Thermal transport in van der Waals solids from first-principles calculations. *Phys. Rev. B* **2016,** *94* (11), 115205.
(62) Yan, X.-J.; Lv, Y.-Y.; Li, L.; Li, X.; Yao, S.-H.; Chen, Y.-B.; Liu, X.-P.; Lu, H.; Lu, M.-H.; Chen, Y.-F., Investigation on the phase-transition-induced hysteresis in the thermal transport along the c-axis of $MoTe_2$. *npj Quantum Mater.* **2017,** *2* (1), 31.
(63) Li, H.; Pandey, T.; Jiang, Y.; Gu, X.; Lindsay, L.; Koh, Y. K., Origins of heat transport anisotropy in $MoTe_2$ and other bulk van der Waals materials. *Mater. Today Phys.* **2023,** *37*, 101196.